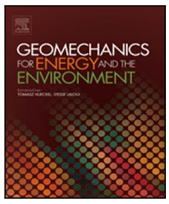
Geomechanics for Energy and the Environment 40 (2024) 100608



Contents lists available at ScienceDirect

Geomechanics for Energy and the Environment

journal homepage: www.elsevier.com/locate/gete



Numerical modeling of hydro-mechanical processes during hydraulic testing of pre-existing fractures at the Grimsel Test Site, Switzerland

Josselin Ouf [a,b,*], Kavan Khaledi [c], Philip J. Vardon [b], Wen Luo [a,b], Mohammadreza Jalali [a], Florian Amann [a,c]

[a] Chair of Engineering Geology and Hydrogeology, RWTH Aachen, Aachen, 52064, Germany
[b] Faculty of Civil Engineering and Geosciences, Delft University of Technology, Delft, 2628 CN, The Netherlands
[c] Fraunhofer Institute for Energy Infrastructures and Geothermal Systems, Aachen, 52062, Germany

ARTICLE INFO

Editors-in-Chief:
Professor Lyesse Laloui and Professor Tomasz Hueckel

Keywords:
Enhanced geothermal system
Hydraulic stimulation
Numerical modeling
Permeability enhancement

ABSTRACT

This study presents a fully coupled hydro-mechanical framework for modeling hydraulic shearing in a mesoscale reservoir located at the Grimsel Test Site, Switzerland. The experiment was conducted on a ductile–brittle fault embedded in low-permeable granite. We observe that normal fracture opening increases flow channel recoverably, while fracture sliding locks asperities leading to a non-recoverable increase in flow. To couple these processes, we use a poro-elasto-plastic constitutive framework and employ a permeability function that depends on several parameters, such as dilation angle, in-situ stresses, residual aperture and maximum aperture. Our results capture the recorded pressure responses well, and indicate that the permeability changes by one order of magnitude during the experiment.

1. Introduction

In deep geothermal systems, fluid predominantly flows through the network of fractures rather than directly through the host rock. These pre-existing fractures serve as the primary conduits for fluid movement between the injection and extraction wells. The fracture network is limiting the ability of a reservoir to carry enough heat flow[1] and fluid flow to be economically viable.[2] The permeability at these depths is often less than 10^{-16} m^2,[3] making it difficult to achieve an economically viable flow rates in the reservoir. To enhance the permeability in fractures at these depths, hydraulic stimulation can be employed. Such systems are referred to as Enhanced Geothermal Energy (EGS) systems.

Hydraulic stimulation for EGS includes the creation of new fractures due to hydraulic fracturing (HF) and/or dilation of existing fractures due to hydraulic shearing (HS). In HF, a fluid is injected into the rock until it fails under tensile opening, causing the creation of new cracks and the extension of existing ones. Proppants might be utilized to maintain these fractures open. In contrast, HS opens existing fractures by injecting fluid. Due to anisotropic stress conditions, natural rough fractures which support shear stresses may dilate upon hydraulic shearing and interlock once the fluid injection stops.[4,5] Studies by Refs. 6, 7 have shown that both HS and HF processes share common mechanisms, although one mechanism may prevail over the other. Our study focuses exclusively on Hydraulic Testing of Pre-existing Fractures (HTPF). Notably, our proposed framework concentrates on modeling HS, with the modeling of HF being beyond the scope of this paper.

On the laboratory scale, considerable research efforts have been devoted to investigating the correlation between effective stress and permeability in fractures. These studies involved conducting laboratory-scale tests, which subsequently yielded empirical relationships widely employed in practical applications.[8–11] Meso-scale (decameter scale) reservoirs were studied to bridge laboratory test scale to reservoir scale, which contribute to improving the understanding of fracture hydraulics and mechanics during stimulation.[12–14] Petty et al.[15] explore the responses of different fractures to different injection scenarios. In a separate study, Krietsch et al.[16] found that these tests provided valuable insights into water circulation, rock deformation, and seismic activity triggered by stimulation. Guglielmi et al.[17] demonstrates on a meso-scale that minor slip movements, typically sub-millimeter in size, lead to substantial increases in permeability. Rutqvist et al.[18] shows that stress and permeability relationships are scale dependent. Zimmermann et al.[19] investigated the fracture conductivity of a real-scale reservoir to gain insights into its long-term injectivity. Recently, Kukkonen et al.[20] stimulate fractures at a depth of 6 km, the permeability was almost fully recovered, with only minor permeability gain upon pressure release.

* Corresponding author at: Chair of Engineering Geology and Hydrogeology, RWTH Aachen, Aachen, 52064, Germany.
E-mail address: j.ouf@tudelft.nl (J. Ouf).

https://doi.org/10.1016/j.gete.2024.100608
Received 18 March 2024; Received in revised form 2 October 2024; Accepted 12 October 2024
Available online 4 November 2024
2352-3808/© 2024 The Authors. Published by Elsevier Ltd. This is an open access article under the CC BY license (http://creativecommons.org/licenses/by/4.0/).

Numerical modeling plays a crucial role in enhancing our understanding of hydraulic stimulation mechanisms. It allows for the estimation of fracture properties through the calibration of numerical models, including fracture normal and shear stiffnesses, as well as the dilation angle. Several EGS project sites have been investigated using numerical modeling techniques. Notable examples include Soults-sous-Foret in France,[21] Fenton Hill in New Mexico, USA,[22] GroßSchönebeck in Germany,[23] and Pohang in South Korea.[24]

Fracture stimulation, induced by water injection, has notable effects on porosity, intrinsic permeability, and local effective stress. In addressing fracture problems, two primary categories of numerical approaches are employed: the continuum and discontinuum representation of fractures. Rutqvist et al.[25] conducted a comparative study on fracture stimulation techniques, evaluating both continuum and discontinuum methods. Their findings indicate that both approaches adequately reproduce the key hydro-mechanical processes taking place within the faults. The implicit representation of fractures captures the impact of fractures by using an equivalent porous media. Various examples of well-known codes which utilize this approach are OpenGeoSys,[26] MOOSE framework,[27] TOUGH-FLAC[28,29] and CODE_BRIGHT.[30] Conversely, the explicit representation of fractures attempt to more realistically include the geometry and impact of fractures, and almost always require some special treatment. Notable examples of these techniques are FEM-DEM/cohesive zone modeling,[31,32] (2) Discrete Fracture Network using interface elements,[7] (3) Embedded lower dimensional elements[33] which are employed for explicit fracture modeling.

In order to attain a more comprehensive understanding of the processes underpinning hydraulic shearing on a broader scale, several in-situ investigations have been undertaken, for example, the In-situ Stimulation and Circulation (ISC) experiments at the Grimsel Test Site in Switzerland.[34–36] These investigations encompassed a range of tests, including hydraulic fracturing and hydraulic shearing, aimed to improve the understanding on fault responses under varying hydraulic stimulation conditions. By integrating the hydromechanical responses of the rock mass, these studies have significantly deepened our understanding of the intricate reactions of faults when subjected to hydraulic stimulation.

The objective of this work is to numerically replicate a selected stimulation at the Grimsel test site. In this study, a continuous modeling approach is utilized. It considers the fault zone as an equivalent porous media, incorporating both the normal elastic opening of the fracture and the shear-slip dilation that happens during hydraulic shearing. The objective of this study are (i) to accurately reproduce the flow rate and injection pressure at the injection well by including HS processes, (ii) simulating the fracture pressure propagation during stimulation within a fault zone, (iii) to evaluation the model's reliability and predictive capabilities in representing real-world hydraulic shearing scenarios.

2. Grimsel test site

The In-situ Stimulation and Circulation (ISC) experiment at the Grimsel Test Site, located in Switzerland, aims to investigate open questions related to deep geothermal reservoirs. Specifically, the focus is on understanding the interaction among hydraulics, mechanics, and seismicity of the rock and fractures during reservoir stimulations, using the site as a decameter-scale analog reservoir.[34] To accomplish this, the experiment is conducted under various stress states and hydraulic conditions and monitored through a combination of geophysical, hydrological, and geomechanical techniques.

The Grimsel test site is located within two granite units, the Grimsel Granodiorite and Central Aar Granite, and is situated approximately 480 m below the surface. Fig. 1 shows the investigated volume of the ISC contains two sets of shear zones, namely the ductile shear zones S1.1, S1.2, S1.3, and the brittle-ductile shear zones S3.1 and S3.2.[37] The investigation revealed the presence of three S1 shear zones and two S3 shear zones, which have an average orientation of 142/77 (dip direction/dip) and 183/65, respectively.[38]

Furthermore, the S1 and S3 shear zones are identifiable from the surface and can be traced back to a distance of approximately 500 m.[39] The average thickness of S1 ranges from 173 to 1670 mm, while S3 ranges from 38 to 312 mm.[36] The investigated ISC volume is intersected by two tunnels, the AU-tunnel and VE-tunnel. These tunnels were excavated in 1983. Additionally, the observed in-situ pressure in the experimental rock volume of the ISC is around 0.2–0.3 MPa, as a result of long-term drainage of the nearby tunnel.[36]

An extensive campaign to characterize the in-situ stress conditions was conducted on the site.[38] The principal stress obtained from inverting strains and additional constraints from hydraulic fracturing give on average; σ_1 = 13 MPa 135/15 (dip direction/dip), σ_2 = 8 MPa 21/43, σ_3 = 6.25 MPa 234/33. The complete GTS data can be found at the following link: https://doi.org/10.3929/ethz-b-000276170.[40]

Table 1
Injection steps within cycle 4 of HS1.

Step	Control	Value	Duration
Step 1	Pressure control	2.32 MPa	592.5 s
Step 2	Pressure control	3.07 MPa	677 s
Step 3	Pressure control	3.51 MPa	450 s
Step 4	Pressure control	4.27 MPa	365 s
Shut-in	–	–	335 s
Step 5	Flow rate control	15 l/min	340 s
Step 6	Flow rate control	25 l/min	308 s
Shut-in	–	–	760 s

3. HS1 stimulation

The HS1 experiment was carried out on February 15, 2017, in the injection borehole INJ2 with the objective to increase the permeability by stimulating the ductile shear zone S1.3 with high pressure injections using a straddle packer system. An additional fracture pressure monitoring system, labeled PRP2, was located 10.72 m from the injection point.[16]

The injection protocol comprised four cycles, with the first two cycles serving as pre-stimulation phases (i.e. two consecutive pressure controlled HTPF tests (hydraulic testing of pre-existing fractures)), with the objectives: (1) to break down cohesive bonds (2) to reopen existing fractures and (3) to determine the initial injectivity and normal stress across the fault zone. The third cycle, referred to as the main stimulation phase, was flow rate controlled and caused the fault zone to open and shear. Injection pressure reduction during flow rate increase during the third stimulation cycle suggested a mixed mode response between hydraulic shearing and hydraulic fracturing.[16] The final cycle (i.e. a pressure controlled HTPF test) aimed to determine the final injectivity and potential changes in normal stress conditions. This study specifically focuses on the last cycle (Cycle 4). The comprehensive details of stimulation process can be found in the Refs. 16, 41.

The various injection steps of cycle 4 are illustrated in Fig. 2, with a summary of these steps is provided in Table 1, highlighting the parameters controlled. In total, cycle 4 consists of six steps and includes two shut-in periods (i.e. injection is temporarily stopped).

4. Modeling approach

4.1. Fully coupled numerical simulator

The primary objective of this study is to replicate the fracture behavior observed during the cycle 4 injection of the HS1 experiment. The numerical model was developed using the Multiphysics Object-Oriented Simulation Environment (MOOSE) framework,[27] which is an open-source finite element method (FEM) platform created by Idaho National Laboratories. This framework offers a flexible and hybrid parallel

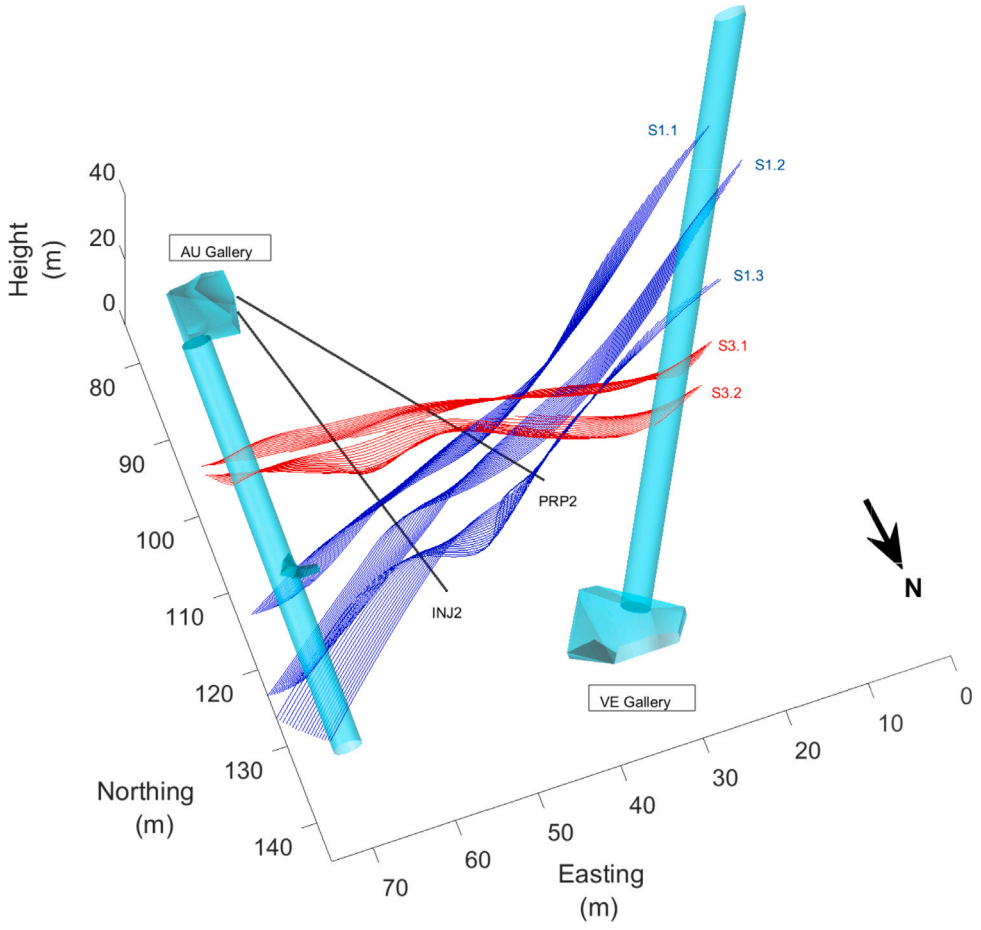


Fig. 1. Grimsel In-situ stimulation and circulation test site — Modified after Ref. 36.

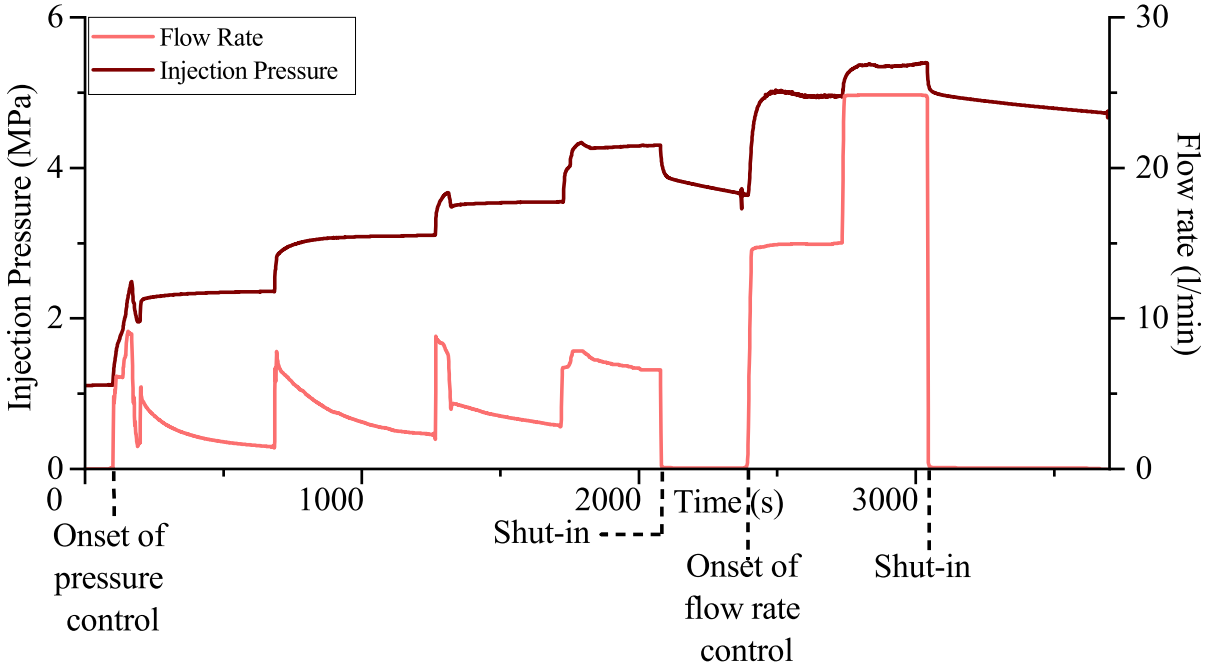


Fig. 2. In-situ injection INJ2: Six injection steps of cycle 4 Post-Stimulation Phase — Modified from Ref. 41.

Table 2
Hydromechanical properties of the model.

Parameters	Symbol	Granite bulk	Fault zone
Geomechanical			
Biot coefficient	(α_b)	1	1
Young Modulus	(E)	47 GPa[a]	30 GPa[a]
Poisson's ratio	(ν)	0.3[a]	0.25[a]
Rock density	(ρ_r)	2640 kg/m^3[a]	2640 kg/m^3[a]
Porosity	(n)	1%[b]	75%
Cohesion	(c)	–	0[c]
Friction angle	(ϕ_r)	–	25°[b]
Dilation angle	(ψ)	–	24°
Hydrogeological			
Permeability	(k)	(k_{bulk}) 10^{-22} m^2[b]	(k_{frac}) variable
Fluid density	(ρ_f)	1000 kg/m^3[d]	1000 kg/m^3[d]
Fluid viscosity	(μ_f)	10^{-9} MPa s[d]	10^{-9} MPa s[d]
Fluid bulk modulus	(K_f)	2 GPa[d]	2 GPa[d]

[a] Properties were adopted from Ref. 40.
[b] Properties were adopted from Ref. 46.
[c] Properties were adopted from Nagra NIB 95-062.
[d] Properties were adopted from Ref. 16.

environment designed for solving multiphysics and multi-component problems in an implicit manner. MOOSE relies on advanced mesh libraries such as libMesh that provide support for adaptive mesh refinement (AMR) computations in parallel.[42] It relies on PETSc for the scalable (parallel) solution of scientific applications modeled by partial differential equations.[43]

An Equivalent Continuum Modeling approach (ECM) was utilized to characterize the hydro-mechanical processes within pre-existing fractures, eliminating the need for computationally intensive treatments such as solving mechanical contact problems. This simplifies the adoption of the approaches explored here. ECM is able to deliver a fully coupled solution and a 3D approach, facilitating a more realistic capture of flow rates while eliminating simplifications such as plain strain or stress. The ECM approach facilitates the solution of fully coupled multi-physics problems with greater ease compared to other methods. Specifically, ECM enables the solution of the kernel in an unstaggered scheme, which is notably more complex when using a discontinuum approach. As a result, the approaches explored in this study have the potential for widespread adoption due to their enhanced efficiency and applicability.

In this method, the fracture was represented as a finite-thickness porous medium with equivalent hydro-mechanical properties, while the intact rock was treated as a low-permeability material. To account for changes in permeability within the fracture zone, an aperture-dependent permeability function was employed. The fracture permeability model was integrated into the multi-physics finite element code MOOSE framework,[44,45] with additional support from the PorousFlow and TensorMechanics modules to solve the coupled hydro-mechanical equations.

4.2. Model set up

The modeling domain was 90 m × 90 m × 50 m (see Fig. 3), with only the S1.3 fault and the bulk rock modeled, and inclusion of the injection point INJ2. Pore pressures are extracted at the location of the PRP2 fracture pressure probe. According to Krietsch et al.[36], the fault width in the model was assumed to be 80 centimeters with a dip direction/dip of 142/77. The positive Y-axis is aligned with the North direction and the positive X-axis with the East direction, while the positive Z-axis points upwards Fig. 3.

The tunnels present at the test sites were not modeled. Hydraulically, the fault zone was represented as a permeable porous medium, whose permeability depends on an aperture function (see Section 4.4.1). Mechanically, the stress–strain relationship in the fault zone was based on an elasto-plastic Mohr–Coulomb law, softening is not included in this framework. The host rock permeability was assumed to be constant (i.e. stress independent). The stress–strain relationships of the host rock was assumed to be linear elastic (i.e. Hooke's law with Young's modulus E and Poisson's ratio ν). The injection process was simulated using a single point (0D element) positioned at the location of INJ2. The fault pressure was tracked at a node located at the same position as probe PRP2, which was 10.72 m away from INJ2 Fig. 3. The model is considered isothermal, with both the bulk rock and fault zone assumed to be fully saturated. The hydraulic boundary conditions were established for granite rock with no-flow boundaries, whereas the fault zone was assigned a boundary condition of 1.17 MPa water pressure matching the initial measured in situ pressures. Consequently, the fracture accommodated leak-off. The initial water pressure was 1.17 MPa in the fault zone and 0.25 MPa in the host rock. Both initial and boundary condition are based on Refs. 36, 41. The mechanical boundary conditions were set as no displacement boundaries in the direction normal to the domain boundaries Fig. 3. The initial stress tensor used was adapted from Ref. 38, and reported in Section 2, and gravity is not included in the model, due to the limited size and high water pressures. The model boundaries (vertical faces) are perpendicular to the principal stress directions. The neglect of gravity is also present in other fracture stimulation studies with high dip angles, such as 65° in Rutqvist et al.[25] and 70 to 90° in Cappa et al.[47]

Table 3
Parameters of the permeability function for the fault zone S1.3.

Parameters	Symbol	Fault zone
Initial aperture	(b_{ini})	17 (μm)
Maximum elastic aperture	(b_{max})	800 (μm)
Stress dependency	(α)	0.275 (MPa^{-1})
Fracture spacing	(s_f)	1 (m^{-1})

Fracture zone homogenization can be idealized as an equivalent porous medium in the case of GTS ductile shear zone due to the small variation in permeability within the fault zone, as discussed by Wenning et al.[48] Assuming linear flow and homogenization over the entire interval, the continuum equivalent porous media was reproduced with the fault zone width and fault zone properties given by Doetsch et al.[40] Properties for the host rock and fracture zone are summarized in Table 2. The parameters used in the Table 3 are parameters of the permeability function for the fault zone S1.3. They are calibrated to reproduce as closely as possible the observations. The initial aperture was assumed 20 μm which is based on the measured hydraulic conductivity of 7×10^{-9} m/s.[49] The parameters used to calibrate are non-unique. The value fault zone contains a single fracture as suggested by the geophysics investigation.[50] We reproduced the injection scenario following the protocol shown in Table 1. The simulation began 100 s before the start of injection cycle 4. The pressure-controlled injection was carried out in four steps from 100 to 2075 s, while the flow rate was monitored. The injection was stopped between 2075 s and 2445 s followed by the two flow rate controlled steps. During the flow rate control phase from 2445 s to 3025 s, fracture pressure was monitored. The injection was stopped at 3025 s, and the stimulation was completed at 3800 s.

4.3. Mechanical formulations

The subsequent equation is valid across the entirety of the domain (including both intact rock and fractures) to maintain the equilibrium of linear momentum, with gravitational forces and inertia effects disregarded.

$$\nabla \cdot \boldsymbol{\sigma} = 0. \tag{1}$$

In the given equation, $\boldsymbol{\sigma}$ is determined by the effective stress $\boldsymbol{\sigma}'$ and the pore pressure p_f using Biot's effective stress principle (expressed

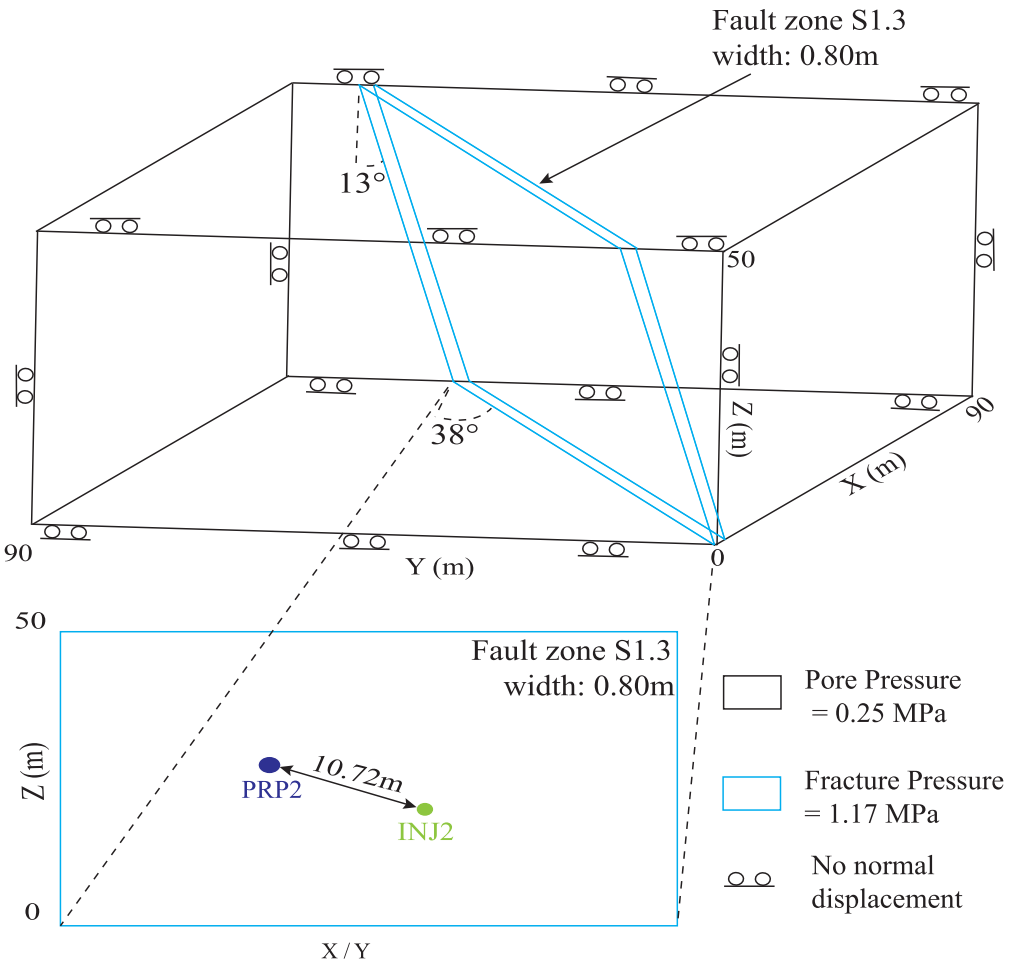


Fig. 3. Numerical model with boundary conditions and location of PRP2 and INJ2.

as $\boldsymbol{\sigma} = \boldsymbol{\sigma}' - \alpha_b p_f \boldsymbol{I}$, where α_b denotes the Biot coefficient). The stress tensor is negative for compressive stress and pressure is positive in compression.

The Mohr–Coulomb yield criterion with constant parameters (no hardening and no softening), marking the onset of plastic shear deformation, is typically defined as follows:

$$\tau = \tan\phi\ \sigma_n' + c \tag{2}$$

where, τ is the shear stress, ϕ is friction angle, σ_n' is the effective normal stress. It should be noted that the above formulation of Mohr–Coulomb does not take into account the fracture orientation.

Shear failure induced dilation is represented by the dilation angle, ψ, which controls the magnitude of the volumetric strain during plastic deformation. The Mohr–Coulomb plastic strain is generally defined as follows:

$$\dot{\epsilon}^p = \lambda \frac{\partial g}{\partial \sigma'} \tag{3}$$

where, $\dot{\epsilon}^p$ is the plastic strain rate, λ is the Lagrange multiplier and g the plastic flow potential. The plastic flow potential in Mohr–Coulomb is generally defined as:

$$g = \tan\psi\ \sigma_n' + c \tag{4}$$

where, τ is the shear stress and σ_n' is the effective normal stress on the fracture plane. The parameters ψ and c are the dilation angle and the cohesion, respectively.

4.4. Hydraulic formulation

The typical formulation for the liquid mass balance in a porous medium is commonly expressed as:

$$\frac{\partial(n\ \rho_f)}{\partial t} + (n\ \rho_f)\frac{\partial \varepsilon_{vol}}{\partial t} = -\boldsymbol{\nabla}\cdot \boldsymbol{q}_f + q^*, \tag{5}$$

where n is the porosity, ρ_f denotes the fluid density, v_s is the velocity of the porous solid skeleton, $\boldsymbol{q}_f$ is the Darcy flux and q^* is the injection source term. The variable ε_{vol} signifies volumetric strain, serving as a connecting factor that demonstrates the influence of mechanical deformation on water pressure. This equation considers changes in porosity, which result in additional fluid storage and alterations in Darcy velocity. These factors are significant in influencing the reactivation front within the fault.[51]

The generalized Darcy's law was used to describe the water flux denoted $\boldsymbol{q}_f$ in Eq. (5) (neglecting gravitational pressure gradient):

$$\boldsymbol{q}_f = -\rho_f \frac{\boldsymbol{k}}{\mu_f}(\boldsymbol{\nabla} p_f) \tag{6}$$

where ρ_f is the fluid density, $\boldsymbol{k}$ is the intrinsic permeability tensor of the medium, μ_f is the dynamic viscosity of water, p_f is the pore pressure.

4.4.1. Permeability function

The permeability of the fracture zone here follows the cubic law,[52,53] given as:

$$\boldsymbol{k} = \frac{b_h^3}{12} s_f \tag{7}$$

where b_h represents the total hydraulic aperture and s_f fracture spacing.

The reactivation of fractures during stimulation initially results in an opening due to a decrease in effective normal stress.[10] Additionally, the permeability of a fracture may further increase when it dilates upon shearing.[54]

To comprehensively account for the combined effects of elastic opening and shear dilation on aperture change, it is necessary to consider variations in fracture aperture as a function of both, effective stress and plastic shear strain. The total change in fracture aperture can be expressed as:

$$b_h = b_{normal} + b_{shear} \tag{8}$$

where, b_h represents the total hydraulic aperture in Eq. (7), b_{normal} denotes for the normal opening, and b_{shear} corresponds to the shear-induced aperture change. By considering the sum of these components, a comprehensive understanding of the aperture change in the fracture can be achieved.

The relationship between recoverable normal opening, confining pressure, and injection pressure has been established by Refs. 55, 56. Their studies illustrated that elastic normal opening is exponential. Subsequent work by Ref. 57 corroborated the accuracy of this function through comprehensive laboratory data analysis. The fracture recoverable normal opening can be expressed as:

$$b_{normal} = b_{ini} + b_{el} \tag{9}$$

where, b_{ini} denotes the initial aperture and b_{el} represents the elastic opening.

The relationship between effective normal stress (σ'_n) and normal opening proposed by Rutqvist and Tsang[56] is given as:

$$b_{el} = b_{max} \exp(-\alpha \sigma'_n) \tag{10}$$

where, b_{max} indicates the maximum aperture and α represents the stress dependency.

The enhancement of permeability due to shear is incorporated through a shear-induced aperture change. Hsiung et al.[58] derived a shear aperture function based on plastic shear strain and dilation. In a similar fashion, Rinaldi et al.[22] proposed a shear-induced aperture function expressed as:

$$b_{shear} = \frac{\epsilon^p_{tangential} \tan(\psi)}{s_f} \tag{11}$$

where, $\epsilon^p_{tangential}$ is the projected plastic strain tangential to the normal of the fault plane, ψ denotes the dilation angle, and s_f represents the fracture spacing.

The interaction between hydraulics and mechanics occurs through several mechanisms: the effective stress concept outlined in Eq. (1), $\frac{\partial \varepsilon_{vol}}{\partial t}$ this terms represents the impact of volumetric strain rate on the fluid pressure in Eq. (5), and changes in permeability as depicted in Eq. (7).

This permeability function, along with an equivalent continuum modeling approach for the fault zone, has been successfully applied in modeling hydraulic shearing and in matching granitic EGS laboratory experiments and field studies conducted by Refs. 22, 24, 59, 60.

4.5. 3D FE modeling of the experiments

The mesh within the fault zone was finer compared to the host rock and further refined between PRP2 and INJ2. The whole model consists of ca. 120 000 nodes and ca. 710 000 elements Fig. 4. We employed the Galerkin finite element method with first-order Lagrange shape functions. Quadrature techniques, primarily Gaussian Quadrature, were used for numerical integration over the reference element. To mitigate volumetric locking, we utilized the b-bar approach within the MOOSE framework, as elaborated in the provided link MOOSE SolidMechanics. In addressing concerns about shear locking, we kept element aspect ratios close to 1 throughout our investigations. Additionally, we exercised caution in determining fracture thickness and final mesh count to avoid very thin elements that might introduce distortion and unwanted numerical artifacts.

Fig. 5 highlights the model's sensitivity to variations in mesh density. We evaluated the maximum injection pressure response at INJ2 across six steps. We have increased the number of elements and nodes only in the refined area, which is shown in Fig. 4. As the number of elements increases, the accuracy of the model improves. Fig. 5 illustrate the convergence of the maximum pressure and plastic tangential strain response with increasing mesh density. Convergence is achieved with 508 132 tetrahedral elements, and the final model, with 715 056 tetrahedral elements, is considered the most accurate. To prevent distortion and numerical artifacts, further increases in the number of elements were avoided. With a stable plastic tangential strain and pressure response influenced by permeability and plastic properties the model appears to be appropriately meshed.

Fig. 6 shows the evolution of tangential plastic strain at different elements. Mechanical convergence is again achieved at 508 132 tetrahedral elements. Fig. 6b and c illustrate the same tangential plastic strain pattern across the fault.

5. Simulation results

In this section, we present the numerical results of the simulation. The simulation used Table 1 as input, with the first four steps modeled for pressure control and steps five and six for flow rate control. The experimental results and associated calibrated numerical results are shown in Fig. 7. The first four steps of the injection were modeled as pressure controlled steps, and therefore match the experimental results closely (shown in Fig. 7-a). The corresponding flow rates during these steps (Fig. 7-b) showed a sudden increase during the first three steps, followed by reaching a steady state. In contrast, the experimental results show a similar, but slightly higher, initial increase in flow rate, which then more gradually decreased in a hyperbolic manner until a steady state was reached at a value which matches well the numerical results. In the fourth step, the flow rate exhibits a more pronounced increase and subsequently undergoes a more minor decay before reaching a steady state. This is interpreted as the initiation of hydraulic shearing.

During the first shut-in phase, the measured injection pressure exhibited a slight decrease, reaching a value of 3.6 MPa, while numerically, it sharply dropped to 1.84 MPa (Fig. 7-a), most likely due to the model boundary conditions that allow a leak off. The pressure response during the last two steps, under flow rate control, show a good qualitative agreement between the numerical simulation and the field data, albeit with the numerical results requiring a higher injection pressure than in the experiment. At a flow rate of 15 l/min, the injection pressure stabilized at 4.95 MPa in the field and at 5.37 MPa in the numerical simulation. Similarly, at a flow rate of 25 l/min, the injection pressure stabilized at 5.37 MPa in the field and at 6.45 MPa in the numerical simulation. After the final shut-in period, the injection pressure decreases sharply to 2.23 MPa in the numerical simulation, whereas experimentally, it gradually decreased to 4.73 MPa, again probably due to the model boundary conditions.

The pressure monitoring point PR2, shown in Fig. 7-c, shows an excellent general agreement with the experimental results. It initially showed a value of 1.17 MPa, and exhibited a slight increase during the first three steps, both numerically and experimentally. At the end of the third step, the measured pressure reached 1.45 MPa, while the numerical simulation yielded a value of 1.38 MPa. During the fourth step, the fracture pressure increased at higher rates due to shear induced changes in permeability. Numerically, the fracture pressure at PRP2 reached 1.54 MPa, while the on-site measurement was 1.55 MPa. During the first shut-in period, the pressure of the numerical simulation and the actual measured values remained virtually constant. Higher permeability

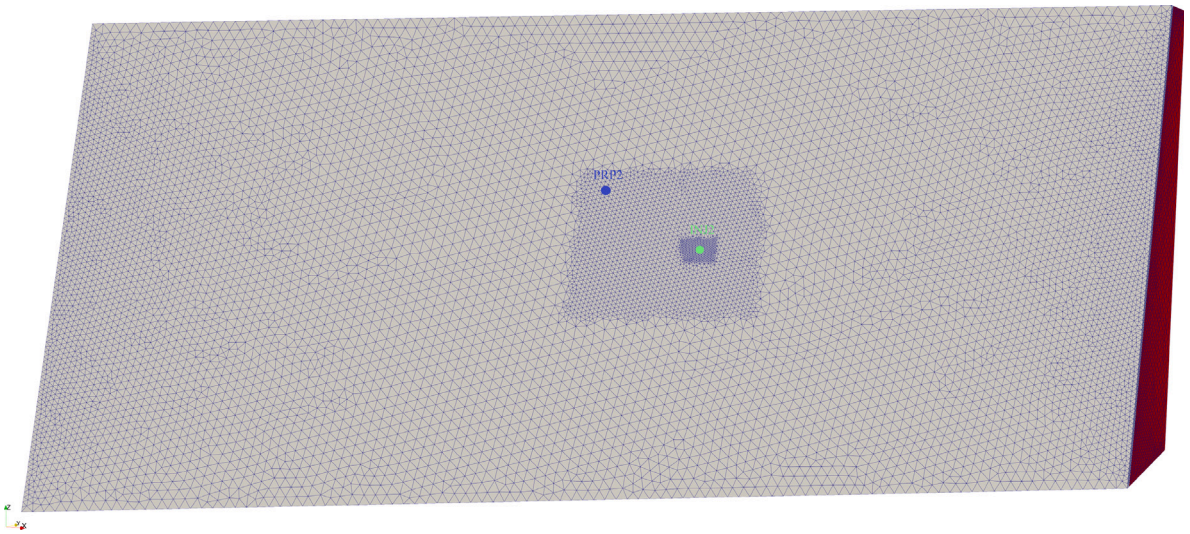


Fig. 4. The mesh of fault within the model showing a refined area around the injection point.

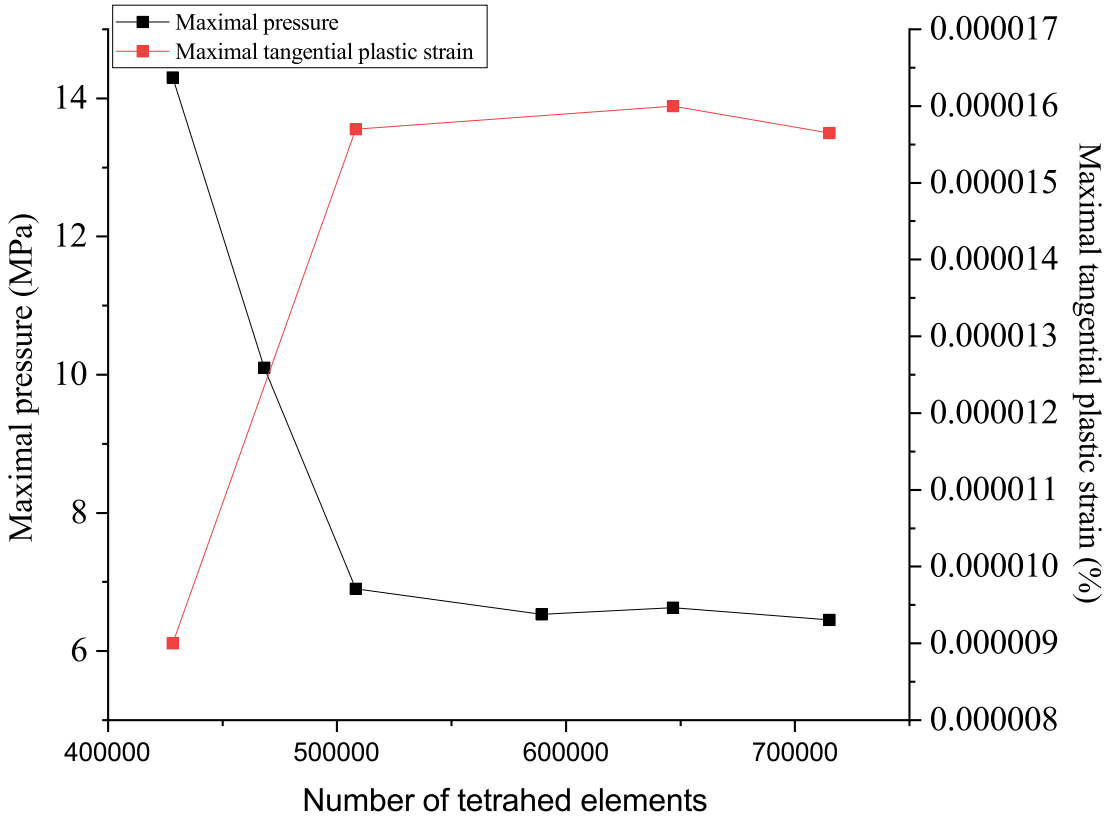


Fig. 5. Mesh convergence study for plastic strain and pore pressure.

changes were observed during the two flow rate injection steps. At the end of the fifth steps, the modeled fracture pressure at PRP2 reached 1.92 MPa, whereas the on-site measurement reached 1.76 MPa. During the final step the on-site fracture pressure reached a maximum of 1.95 MPa, while numerically it increases to 2.21 MPa. During the shut-in period, the on-site fracture pressure remains constant at 1.95 MPa, while numerically it dropped to 1.92 MPa (Fig. 7-c).

The flow rate and pressure at steady state are presented in Fig. 8. We calculated the average flow rate and injection pressure for the final 50 s of each step. As shown in Fig. 8, the numerical simulation accurately captures the behavior up to the fourth step, which are mostly controlled by recoverable normal opening. The last two steps show an approximate match with the numerical flow rate at 5.37 MPa in the fifth step (compared to the experimental value of 4.91 MPa) and at 6.45 MPa during the last step (compared to the experimental value of 5.36 MPa). In the elastic region, up to 3.51 MPa, the relationship between flow rate and pressure was linear, reflecting the linear elastic granite behavior. However, for larger pressures a sharp increase in the relationship between flow rate and fracture pressure was observed. Fig. 8 suggests a jacking pressure between 3.51 and 4.27 MPa.

The presented model shows reversible permeability changes during the initial three steps. Specifically, the numerical analysis shows that the fracture opens in a reversible manner. At this stage, the permeability is solely governed by the elastic deformation, denoted as

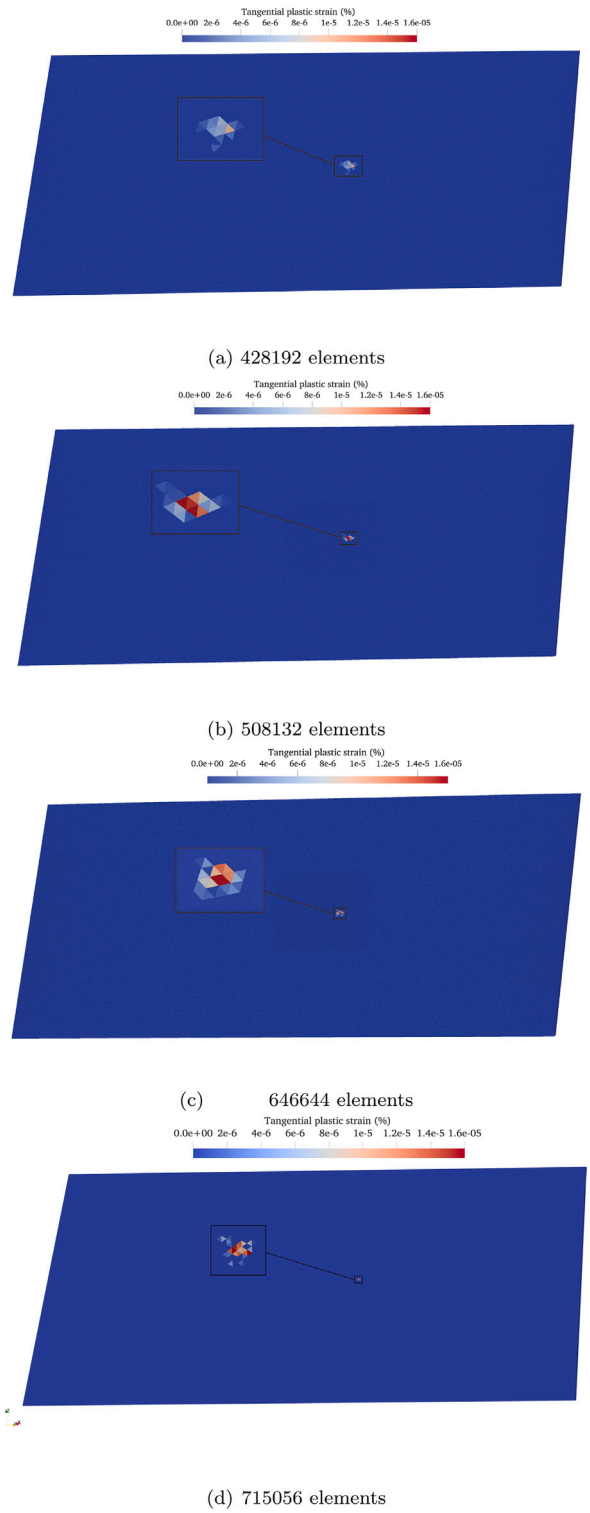


Fig. 6. Tangential plastic strain at mesh density; (a) 428 192 elements (b) 508 132 elements (c) 646 644 elements (d) 715 056 elements.

b_{el}. However, the onset of plasticity was observed when the fracture pressure exceeded 4 MPa. This is numerically represented by sliding and dilation of the fracture. Plastic deformations lead to the creation of irreversible permeability.

Fig. 9-a shows the normal opening (b_{normal}) and shear opening (b_{shear}) of the fault at INJ2. Major fluctuations are observed in the normal opening (b_{normal}), with an initial value of 67.27 μm and a final value of 74.33 μm. The maximum aperture at the highest flow rate was 129.6 μm. Fig. 9-a also suggests that the majority of aperture changes was reversible.

The onset of shear displacement and related aperture changes occurred during the 4th step at 1725 s, coinciding with an injection pressure of 4.27 MPa. At this stage, the shear aperture reached 0.82μm. Subsequently, during the 5th step, the shear aperture further increased to 4.75 μm. In the final step, at a flow rate of 25 l/min, the aperture changes related to shear reached its maximum value of 7.12 μm. Due to irreversible plastic straining of the fault zone, the shear aperture remained (i.e. irreversible) after shut-in, as shown in Fig. 9-a.

Fig. 9-c shows the permeability at INJ2. The initial permeability was 2.53×10^{-14} m^2. Over the first three steps, the permeability increased only due to normal opening, reaching 4.44×10^{-14} m^2 by the end of the third steps. In the fourth step, the permeability increased substantially to a value of 6.24×10^{-13} m^2, mainly due to normal opening with a minor contribution from shear opening. Upon injection pressure release, the permeability decreased to 3.12×10^{-14} m^2. In the fifth step, the simultaneous increase in b_{normal} and b_{shear} led to a permeability of 1.26×10^{-13} m^2. Finally, during the last step, the permeability reached its maximum value of 2.11×10^{-13} m^2. During venting the wellbore, permeability changes were primarily controlled by b_{normal}, and the related permeability at the end of the test was determined to be 4.52×10^{-14} m^2 Fig. 9-c.

At monitoring point PRP2, no changes in shear displacement (b_{shear}) were detected. Initially, the normal opening (b_{normal}) at PRP2 measured 67.27 μm with a corresponding permeability of 2.53×10^{-14} m^2. The evolution of the normal opening was notably influenced by pressure diffusion. Over the first three steps, a slight increase in b_{normal} was observed, reaching 69.74 μm, accompanied by a gradual rise in permeability to 2.85×10^{-14} m^2. Subsequently, during the fourth step, the increase in b_{normal} became more pronounced due to the initiation of hydraulic shearing at INJ2, resulting in a b_{normal} value of 70.80 μm and a permeability of 2.96×10^{-14} m^2. The maximum value of b_{normal} reached 77.13 μm, with a corresponding permeability of 3.86×10^{-14} m^2, observed when the flow rate was 25 l/min. During the second venting phase, the normal opening gradually decreased, reaching a final value of 73.7 μm, with a permeability of 3.32×10^{-14} m^2 Fig. 9-b. Notably, since the fracture pressure did not revert to its initial value, the final b_{normal} value exceeded the initial measurement.

Fig. 10 illustrates the spatial variation of pore pressure in the fault zone, termed the fracture pressure. Each sub-figure represents the fracture pressure at the end of an injection step, showing both a contour plot of the pressure in the fault zone and the values on a section through the fault below (dashed red line). At the end of each injected step, an approximate radial diffusion pattern is shown within the fault. An analytical solution to the radial diffusivity equation for a confined aquifer under semi-steady state conditions[61] is overlain with a solid blue line. This solution uses assumptions that the reservoir is homogeneous in all rock properties, the domain is infinite and isotropic in permeability. Additionally, it assumes that the producing well is completed across the entire formation thickness, ensuring fully radial flow. Furthermore, the formation is considered to be completely saturated with a single fluid. The analytical solution generates a hyperbolic pressure profile in all steps, indicating that the fracture pressure diffuses along the fracture. However, the analytical solution does not stabilize the fracture pressure significantly far away from the injection point. Instead, the fracture pressure decays hyperbolically in all steps until reaching the model's limits. The numerical solution of pressure propagation exhibits a limited radial perturbation of fracture pressure along the fault zone, attributed to the increase in permeability in that zone. Additionally, cross section B-B' in Fig. 10 illustrates radial diffusion in the transversal plane. This radial diffusion in the transversal plane show the same diffusion pattern as the diffusion in the longitudinal plane.

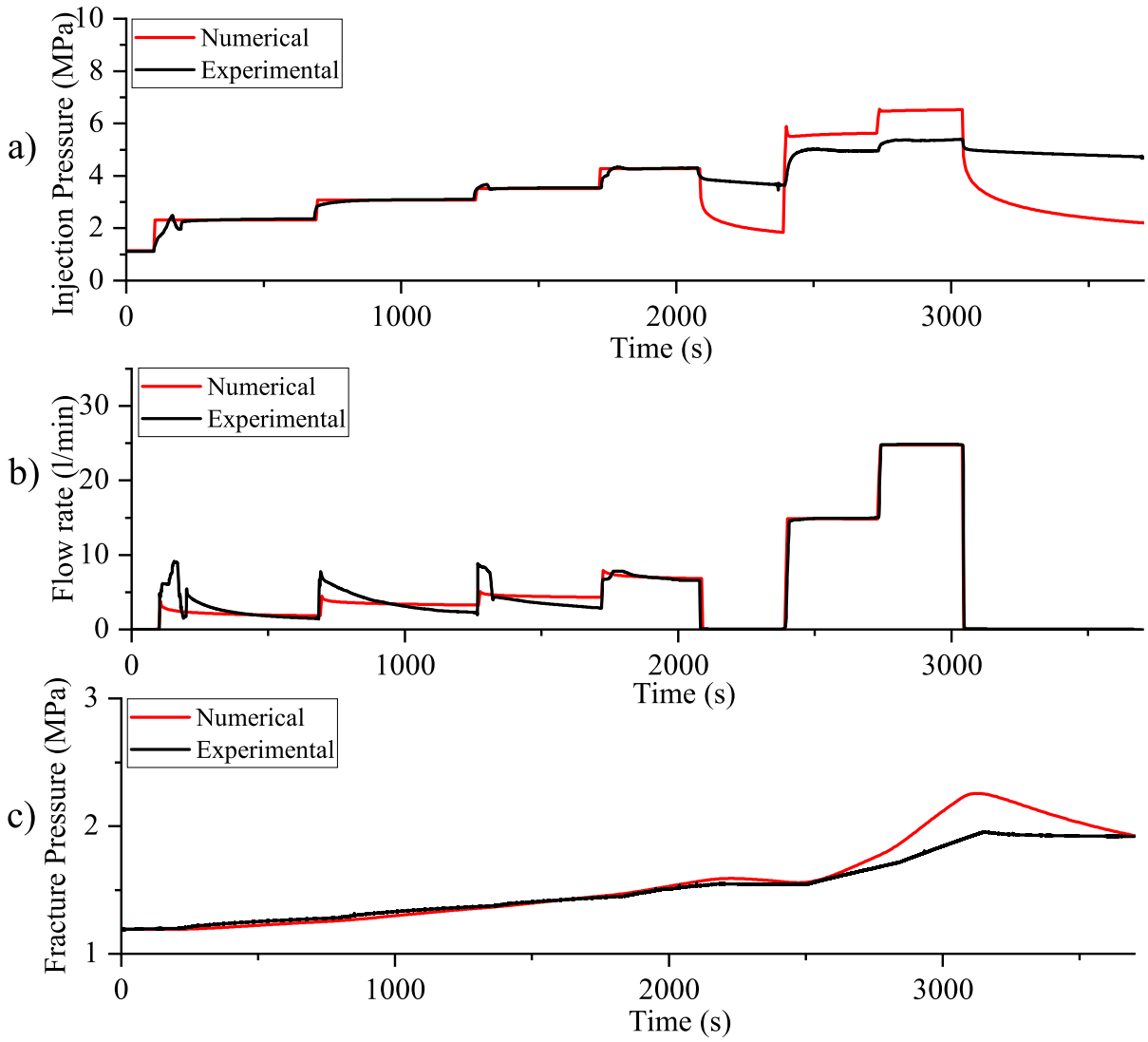


Fig. 7. (a) Injection pressure at INJ2, (b) Flow rate at INJ2, (c) Fracture pressure at PRP2.

The experimental data obtained at PRP2 show strong agreement with both the numerical model and analytical solution illustrated in Fig. 10 across all stages. However, beginning from the fourth stage, stronger disparities emerge between the analytical and numerical solutions regarding fracture pressure around the injection site. This variance becomes more pronounced due to the onset of hydraulic shearing occurring at step 4, and further consequential increases in permeability in this zone. The linear diffusion model does not include a finite domain and the influence of pressure-dependent permeability or aperture increases due to shearing, with only the storage being pressure-dependent. In contrast, the model incorporated the aperture change of the fault with pressure and shear deformation. Consequently, the numerical model predicts a larger area experiencing higher pressures compared to the analytical solution. As the pressure increases, this disparity between the numerical and analytical models further magnifies.

6. Discussion and conclusion

In this paper, we present a model for permeability enhancement during hydraulic stimulation of a meso-scale reservoir. Our model was designed to represent the conditions observed at the Grimsel ISC test site, and specifically the HS1 stimulation test. The proposed permeability function accounts for both recoverable normal opening and unrecoverable shear opening, providing a comprehensive representation of the system. The model deviates from the experimental results during shut in periods, most likely due to the boundary conditions and limited domain of the model.

Specifically, our investigation revealed that for pressures below the jacking pressure, permeability changes occurred exclusively in an elastic manner. Once the jacking pressure was exceeded, the permeability was controlled by both elastic normal opening and fracture sliding. Our model revealed a permeability increase of approximately 1 magnitude, mostly due to recoverable opening.

To further refine our results, the injection system could replicate the behavior of a packer system in the well. This method could enhance our simulation results by increasing the accuracy of flow rate versus injection pressure relationship at the INJ2 borehole. Crack formation and extension which occurred during step 3,[16] which were not integrated into our model, are likely to have impacted the results. These cracks might have a significant influence on injectivity and pressure response and correspond with the mismatch in results in the last two steps. During the last two steps, the injection pressure responses in the numerical model were consistently higher than those observed in the experimental data. A greater fracture opening or additional cracks in our model would align more closely with the experimental results.

We have showcased, supported by reasonable assumptions, the model's capability to capture the transient propagation of pressure

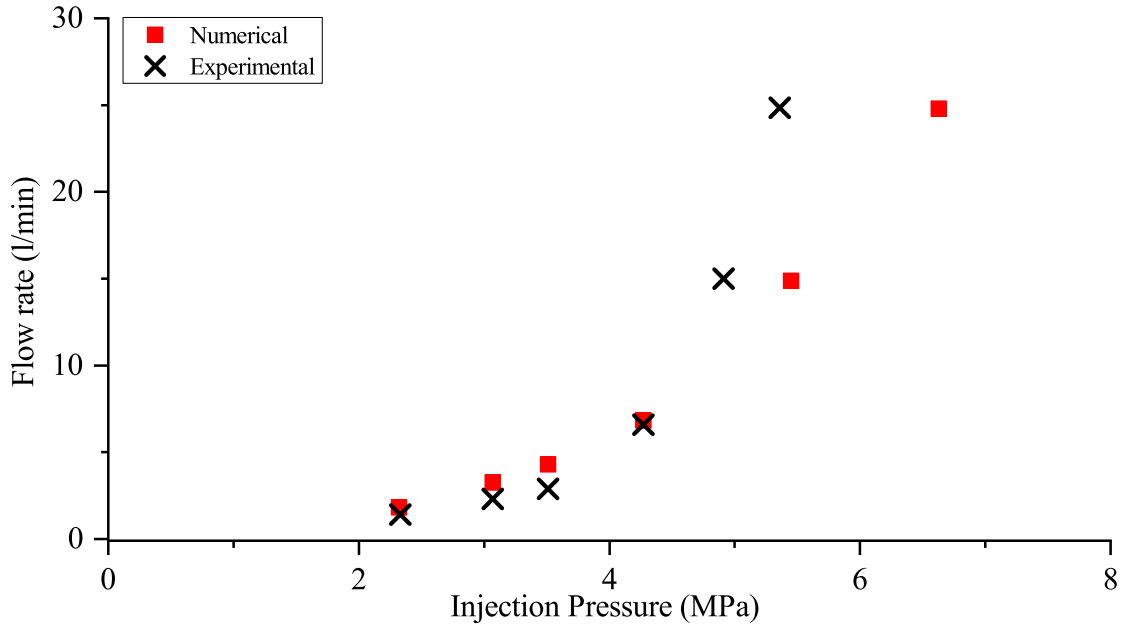


Fig. 8. Flow rate vs. Injection pressure at INJ2.

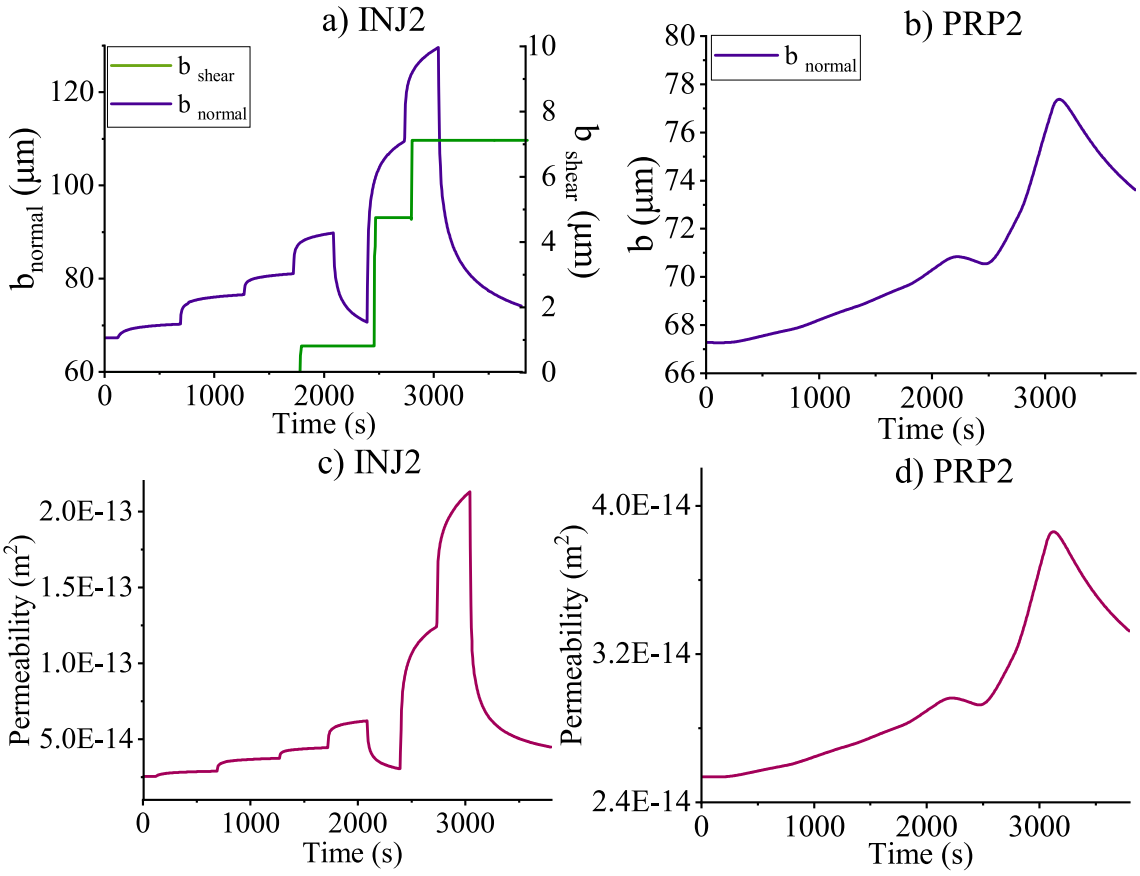


Fig. 9. Fracture permeability and aperture change; (a) Aperture variation over time at INJ2, (b) aperture variation over time at PRP2, (c) permeability change at INJ2, (d) permeability change at PRP2.

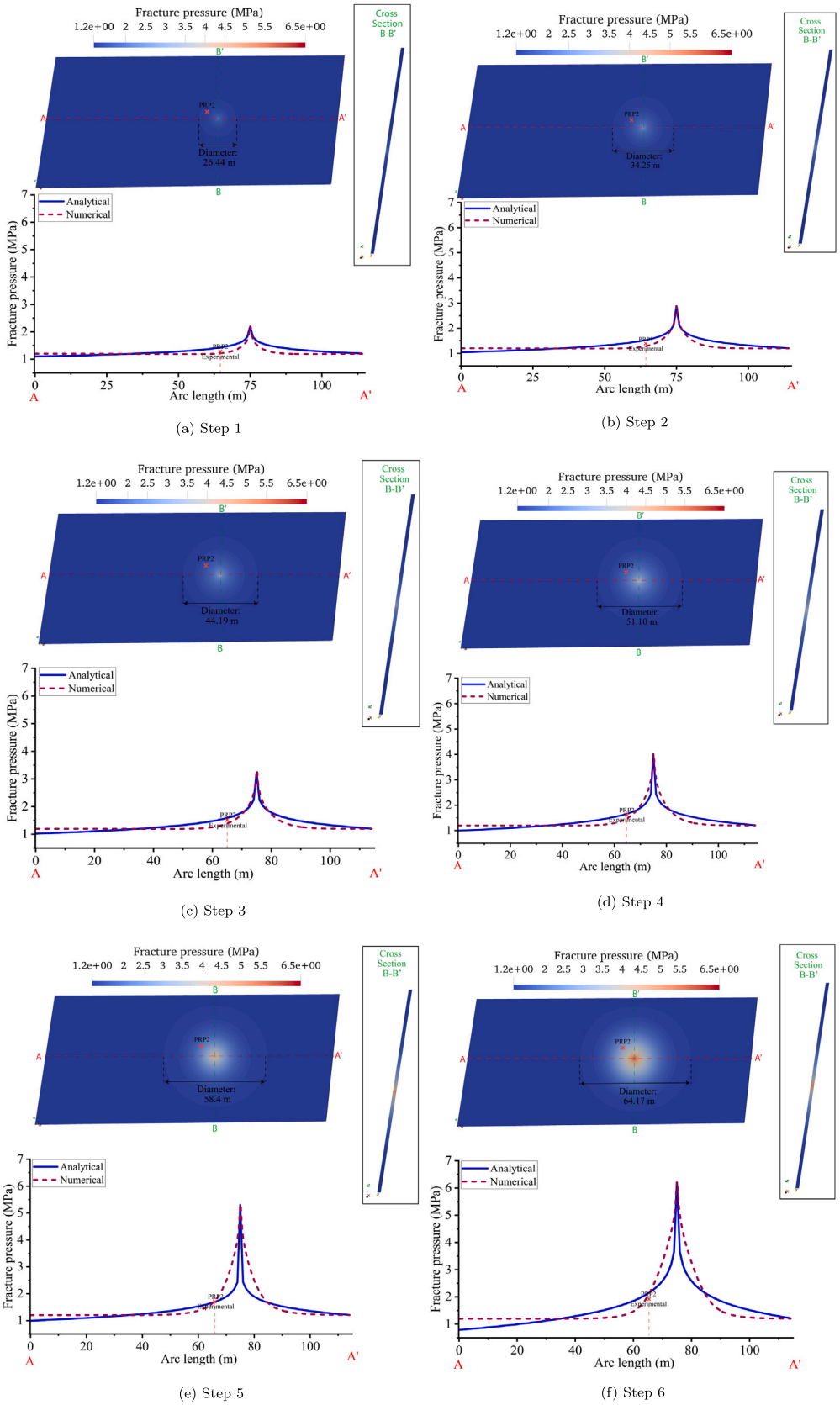


Fig. 10. Fracture pressure at different steps; (a) Step 1 : Injection pressure 2.33 MPa; flow rate 1.82 l/min; time 680 s, (b) Step 2: Injection pressure 3.07 MPa; flow rate 3.26 l/min; time 1260 s, (c) Step 3: Injection pressure 3.51 MPa; flow rate 4.3 l/min; time 1720 s, (d) Step 4: Injection pressure 4.27 MPa; flow rate 6.57 l/min; time 2080 s (e) Step 5: Injection pressure 5.37 MPa; flow rate 15.00 l/min; time 2730 s, (f) Step 6: Injection pressure 6.45 MPa; flow rate 25.00 l/min; time 3000 s.

within the system. At PRP2, we provide evidence of the existence of elastic opening only. The numerical changes of fracture pressure at PRP2 are reproduced accurately. A greater variation in permeability of the fracture would have led to lower fracture pressure during the last two steps. By adequately incorporating this opening phenomenon into the model, we anticipate a less pronounced response in fracture pressure to the injection. Consequently, the fracture pressure at PRP2 would have been diminished, aligning more closely with the site measurements. We demonstrated that the utilization of the radial diffusivity equation for a confined aquifer under semi-steady state condition equation results in a good agreement with the fracture pressure modeled for the first 4 steps, with higher deviation occurring during the last 2 steps.

The significance of hydromechanical interactions in the vicinity of a stimulation campaign is highlighted, which is of particular relevance for Enhanced Geothermal Systems (EGS). The proposed model effectively captures the behavior by integrating elastic and plastic responses that enhance permeability. The Equivalent Continuum Modeling approach enables a solution that can be replicated by engineers providing a realistic representation of the dynamics involved during such operations.

CRediT authorship contribution statement

Josselin Ouf: Writing – review & editing, Writing – original draft, Visualization, Methodology, Investigation, Formal analysis, Data curation, Conceptualization. **Kavan Khaledi:** Visualization, Supervision, Methodology, Investigation, Formal analysis, Data curation, Conceptualization. **Philip J. Vardon:** Writing – original draft, Supervision, Methodology, Formal analysis, Conceptualization. **Wen Luo:** Writing – review & editing, Methodology, Investigation. **Mohammadreza Jalali:** Writing – review & editing, Supervision, Methodology, Investigation. **Florian Amann:** Writing – review & editing, Supervision, Methodology, Investigation, Funding acquisition, Formal analysis, Conceptualization.

Declaration of Generative AI and AI-assisted technologies in the writing process

During the preparation of this work, the authors used Chat GPT - 3.5 in order to improve the text quality and readability. After using this tool/service, the authors reviewed and edited the content as needed and takes full responsibility for the content of the publication.

Declaration of competing interest

The authors declare that they have no known competing financial interests or personal relationships that could have appeared to influence the work reported in this paper.

Acknowledgments

This work is provided under the framework of Efficiency & Safety in Geothermal Operations (EASY-GO) within the IDEA League network. We acknowledging the European Union's Horizon 2020 research and innovation program under the Marie Sklodowska-Curie grant agreement No 956965 for providing funds for the study. We also thanks three anonymous reviewers for their helpful reviews.

Data availability

Data will be made available on request.

References

1. Saar MO. Geothermal heat as a tracer of large-scale groundwater flow and as a means to determine permeability fields. *Hydrogeol J*. 2011;19(1):31.
2. Breede K, Dzebisashvili K, Liu X, Falcone G. A systematic review of enhanced (or engineered) geothermal systems: past, present and future. *Geotherm Energy*. 2013;1:1–27.
3. Manning C, Ingebritsen S. Permeability of the continental crust: Implications of geothermal data and metamorphic systems. *Rev Geophys*. 1999;37(1):127–150.
4. Pine R, Batchelor A. Downward migration of shearing in jointed rock during hydraulic injections. In: *International Journal of Rock Mechanics and Mining Sciences & Geomechanics Abstracts*. Elsevier; 1984:249–263. Vol. 21.
5. Cladouhos T, Petty S, Larson B, Iovenitti J, Livesay B, Baria R. Toward more efficient heat mining: a planned enhanced geothermal system demonstration project. *GRC Trans*. 2009;33:165–170.
6. McClure MW, Horne RN. An investigation of stimulation mechanisms in enhanced geothermal systems. *Int J Rock Mech Min Sci*. 2014;72:242–260.
7. Gischig VS, Preisig G. Hydro-fracturing versus hydro-shearing: a critical assessment of two distinct reservoir stimulation mechanisms. In: *13th ISRM International Congress of Rock Mechanics*. OnePetro; 2015.
8. Barton N. Review of a new shear-strength criterion for rock joints. *Eng Geol*. 1973;7(4):287–332.
9. Goodman R. The mechanical properties of joints. In: *Proc 3rd Int Congr International Society of Rock Mechanics*. 1974:1–7.
10. Bandis S, Lumsden A, Barton N. Fundamentals of rock joint deformation. In: *International Journal of Rock Mechanics and Mining Sciences & Geomechanics Abstracts*. Elsevier; 1983:249–268. Vol. 20.
11. Yeo I, De Freitas M, Zimmerman R. Effect of shear displacement on the aperture and permeability of a rock fracture. *Int J Rock Mech Min Sci*. 1998;35(8):1051–1070.
12. Jung R. Hydraulic in situ investigations of an artificial fracture in the Falkenberg granite. In: *International Journal of Rock Mechanics and Mining Sciences & Geomechanics Abstracts*. Elsevier; 1989:301–308. Vol. 26.
13. Rutqvist J. Determination of hydraulic normal stiffness of fractures in hard rock from well testing. In: *International Journal of Rock Mechanics and Mining Sciences & Geomechanics Abstracts*. Elsevier; 1995:513–523. Vol. 32.
14. Guglielmi Y, Cappa F, Avouac J-P, Henry P, Elsworth D. Seismicity triggered by fluid injection–induced aseismic slip. *Science*. 2015;348(6240):1224–1226.
15. Petty S, Nordin Y, Glassley W, Cladouhos TT, Swyer M. Improving geothermal project economics with multi-zone stimulation: results from the Newberry Volcano EGS demonstration. In: *Proceedings Of the Thirty-Eighth Workshop on Geothermal Reservoir Engineering*. 2013:11–13.
16. Krietsch H, Gischig VS, Doetsch J, Evans KF, Villiger L, Jalali M, Valley B, Löw S, Amann F. Hydromechanical processes and their influence on the stimulation effected volume: observations from a decameter-scale hydraulic stimulation project. *Solid Earth*. 2020;11(5):1699–1729.
17. Guglielmi Y, Birkholzer J, Rutqvist J, Jeanne P, Nussbaum C. Can fault leakage occur before or without reactivation? Results from an in situ fault reactivation experiment at Mont Terri. *Energy Procedia*. 2017;114:3167–3174.
18. Rutqvist J. Fractured rock stress–permeability relationships from in situ data and effects of temperature and chemical–mechanical couplings. *Crustal Permeability*. 2012:65–82.
19. Zimmermann G, Reinicke A. Hydraulic stimulation of a deep sandstone reservoir to develop an enhanced geothermal system: Laboratory and field experiments. *Geothermics*. 2010;39(1):70–77.
20. Kukkonen IT, Heikkinen PJ, Malin PE, Renner J, Dresen G, Karjalainen A, Rytkönen J, Solantie J. Hydraulic conductivity of the crystalline crust: Insights from hydraulic stimulation and induced seismicity of an enhanced geothermal system pilot reservoir at 6 km depth, espoo, southern Finland. *Geothermics*. 2023;112:102743.
21. Baisch S, Vörös R, Rothert E, Stang H, Jung R, Schellschmidt R. A numerical model for fluid injection induced seismicity at Soultz-sous-Forêts. *Int J Rock Mech Min Sci*. 2010;47(3):405–413.
22. Rinaldi AP, Rutqvist J. Joint opening or hydroshearing? Analyzing a fracture zone stimulation at Fenton hill. *Geothermics*. 2019;77:83–98.
23. Blöcher G, Cacace M, Jacquey AB, Zang A, Heidbach O, Hofmann H, Kluge C, Zimmermann G. Evaluating micro-seismic events triggered by reservoir operations at the geothermal site of Groß Schönebeck (Germany). *Rock Mech Rock Eng*. 2018;51:3265–3279.
24. Yoo H, Park S, Xie L, Kim K-I, Min K-B, Rutqvist J, Rinaldi AP. Hydro-mechanical modeling of the first and second hydraulic stimulations in a fractured geothermal reservoir in Pohang, South Korea. *Geothermics*. 2021;89:101982.
25. Rutqvist J, Graupner B, Guglielmi Y, Kim T, Maßmann J, Nguyen TS, Park J-W, Shiu W, Urpi L, Yoon JS, et al An international model comparison study of controlled fault activation experiments in argillaceous claystone at the mont terri laboratory. *Int J Rock Mech Min Sci*. 2020;136:104505.
26. Kolditz O, Bauer S, Bilke L, Böttcher N, Delfs J-O, Fischer T, Görke UJ, Kalbacher T, Kosakowski G, McDermott C, et al OpenGeoSys: an open-source initiative for numerical simulation of thermo-hydro-mechanical/chemical (THM/C) processes in porous media. *Environ Earth Sci*. 2012;67:589–599.

27. Permann CJ, Gaston DR, Andrš D, Carlsen RW, Kong F, Lindsay AD, Miller JM, Peterson JW, Slaughter AE, Stogner RH, Martineau RC. MOOSE: Enabling massively parallel multiphysics simulation. *SoftwareX*. 2020;11:100430. http://dx.doi.org/10.1016/j.softx.2020.100430, URL http://www.sciencedirect.com/science/article/pii/S2352711019302973.
28. Itasca F. *FLAC-Fast Lagrangian Analysis of Continua, Version. 7.0*. Minneapolis: Itasca Consulting Group Inc.; 2011.
29. Rutqvist J. An overview of TOUGH-based geomechanics models. *Comput Geosci*. 2017;108:56–63.
30. Gesto JM, González NA, Olivella S, Vaunat J, Gens A. The structure of code-bright: flowchart and future developments.
31. Lisjak A, Mahabadi O, Kaifosh P, Vietor T, Grasselli G. A preliminary evaluation of an enhanced FDEM code as a tool to simulate hydraulic fracturing in jointed rock masses. In: *ISRM EUROCK*. ISRM; 2014:ISRM–EUROCK.
32. Grasselli G, Lisjak A, Mahabadi OK, Tatone BS. Influence of pre-existing discontinuities and bedding planes on hydraulic fracturing initiation. *Eur J Environ Civ Eng*. 2015;19(5):580–597.
33. Watanabe N, Wang W, Taron J, Görke U, Kolditz O. Lower-dimensional interface elements with local enrichment: application to coupled hydro-mechanical problems in discretely fractured porous media. *Internat J Numer Methods Engrg*. 2012;90(8):1010–1034.
34. Amann F, Gischig V, Evans K, Doetsch J, Jalali R, Valley B, Krietsch H, Dutler N, Villiger L, Brixel B, et al The seismo-hydromechanical behavior during deep geothermal reservoir stimulations: open questions tackled in a decameter-scale in situ stimulation experiment. *Solid Earth*. 2018;9(1):115–137.
35. Jalali M, Klepikova M, Doetsch J, Krietsch H, Brixel B, Dutler N, Gischig V, Amann F. A multi-scale approach to identify and characterize the preferential flow paths of a fractured crystalline rock. In: *ARMA International Discrete Fracture Network Engineering Conference*. ARMA; 2018:D033S020R001.
36. Krietsch H, Doetsch J, Dutler N, Jalali M, Gischig V, Loew S, Amann F. Comprehensive geological dataset describing a crystalline rock mass for hydraulic stimulation experiments. *Sci Data*. 2018;5(1):1–12.
37. Keusen H, Ganguin J, Schuler P, Buletti M. *Grimsel Test Site: Geology*. Tech. Rep.; Nationale Genossenschaft fuer die Lagerung Radioaktiver Abfaelle (NAGRA); 1989.
38. Krietsch H, Gischig V, Evans K, Doetsch J, Dutler NO, Valley B, Amann F. Stress measurements for an in situ stimulation experiment in crystalline rock: integration of induced seismicity, stress relief and hydraulic methods. *Rock Mech Rock Eng*. 2019;52:517–542.
39. Schneeberger R, de La Varga M, Egli D, Berger A, Kober F, Wellmann F, Herwegh M. Methods and uncertainty estimations of 3-D structural modelling in crystalline rocks: a case study. *Solid Earth*. 2017;8(5):987–1002.
40. Doetsch J, Gischig V, Krietsch H, Villiger L, Amann F, Dutler N, Jalali R, Brixel B, Klepikova M, Roques C, et al *Grimsel ISC Experiment Description*. Tech. Rep.; ETH Zurich; 2018.
41. Krietsch H. *Hydro-Mechanical Responses of a Fractured Rock Mass During Decameter-Scale Hydraulic Stimulation Experiments* (Ph.D. thesis). ETH Zurich; 2019.
42. Kirk BS, Peterson JW, Stogner RH, Carey GF. libMesh: a C++ library for parallel adaptive mesh refinement/coarsening simulations. *Eng Comput*. 2006;22:237–254.
43. Balay S, Abhyankar S, Adams M, Brown J, Brune P, Buschelman K, Dalcin L, Eijkhout V, Gropp W, Kaushik D, et al *PETSc Users Manual Revision 3.8*. Tech. Rep.; Office of Scientific and Technical Information (OSTI); 2017.
44. Wilkins A, Green CP, Ennis-King J. PorousFlow: a multiphysics simulation code for coupled problems in porous media. *J Open Sour Softw*. 2020;5(55):2176. http://dx.doi.org/10.21105/joss.02176.
45. Wilkins A, Green CP, Ennis-King J. An open-source multiphysics simulation code for coupled problems in porous media. *Comput Geosci*. 2021;154:104820. http://dx.doi.org/10.1016/j.cageo.2021.104820.
46. Keusen H, Ganguin J, Schuler P, Buletti M. *Felslabor Grimsel Geologie Nagra Technischer Bericht NTB 87-14. 166*. Nagra & Geotest; 1989.
47. Cappa F, Guglielmi Y, Rutqvist J, Tsang C, Thoraval A. Hydromechanical modelling of pulse tests that measure fluid pressure and fracture normal displacement at the Coaraze laboratory site, France. *Int J Rock Mech Min Sci*. 2006;43(7):1062–1082.
48. Wenning QC, Madonna C, de Haller A, Burg J-P. Permeability and seismic velocity anisotropy across a ductile–brittle fault zone in crystalline rock. *Solid Earth*. 2018;9(3):683–698.
49. Brixel B, Klepikova M, Lei Q, Roques C, Jalali MR, Krietsch H, Loew S. Tracking fluid flow in shallow crustal fault zones: 2. Insights from cross-hole forced flow experiments in damage zones. *J Geophys Res: Solid Earth*. 2020;125(4):e2019JB019108.
50. Doetsch J, Krietsch H, Schmelzbach C, Jalali M, Gischig V, Villiger L, Amann F, Maurer H. Characterizing a decametre-scale granitic reservoir using ground-penetrating radar and seismic methods. *Solid Earth*. 2020;11(4):1441–1455.
51. Rutqvist J, Rinaldi AP, Cappa F, Moridis GJ. Modeling of fault activation and seismicity by injection directly into a fault zone associated with hydraulic fracturing of shale-gas reservoirs. *J Pet Sci Eng*. 2015;127:377–386.
52. Snow DT. *A Parallel Plate Model of Fractured Permeable Media*. University of California, Berkeley; 1965.
53. Witherspoon PA, Wang JS, Iwai K, Gale JE. Validity of cubic law for fluid flow in a deformable rock fracture. *Water Resour Res*. 1980;16(6):1016–1024.
54. Barton N, Bandis S, Bakhtar K. Strength, deformation and conductivity coupling of rock joints. In: *International Journal of Rock Mechanics and Mining Sciences & Geomechanics Abstracts*. Elsevier; 1985:121–140. Vol. 22.
55. Louis C, Dessenne J, Feuga B. Interaction between water flow phenomena and the mechanical behavior of soil or rock masses. *Finite Elements Geomech*. 1977:479–511.
56. Rutqvist J, Tsang C-F. Analysis of thermal–hydrologic–mechanical behavior near an emplacement drift at Yucca Mountain. *J Contam Hydrol*. 2003;62:637–652.
57. Liu H-H, Wei M-Y, Rutqvist J. Normal-stress dependence of fracture hydraulic properties including two-phase flow properties. *Hydrogeol J*. 2013;21(2):371.
58. Hsiung S, Chowdhury A, Nataraja M. Numerical simulation of thermal–mechanical processes observed at the drift-scale heater test at Yucca Mountain, Nevada, USA. *Int J Rock Mech Min Sci*. 2005;42(5–6):652–666.
59. Ouf J, Osten J, Luo W, Khaledi K, Jalali M, Vardon PJ, Amann F. Experimental and numerical analysis of injection-induced permeability changes in pre-existing fractures. *Geomech Energy Environ*. 2024;39:100576.
60. Rinaldi AP, Rutqvist J, Sonnenthal EL, Cladouhos TT. Coupled THM modeling of hydroshearing stimulation in tight fractured volcanic rock. *Transp Porous Media*. 2015;108(1):131–150.
61. Dake LP. *Fundamentals of Reservoir Engineering*. Elsevier; 1983.